



# Depth and strain rate-dependent mechanical response of chondrocytes in reserve zone cartilage subjected to compressive loading

Masumeh Kazemi<sup>1</sup> · John L. Williams<sup>1</sup>

Received: 22 December 2020 / Accepted: 31 March 2021 / Published online: 12 April 2021  
© The Author(s), under exclusive licence to Springer-Verlag GmbH Germany, part of Springer Nature 2021

## Abstract

The role of the growth plate reserve zone is not well understood. It has been proposed to serve as a source of stem cells and to produce morphogens that control the alignment of clones in preparation for the transition into the proliferative zone. We hypothesized that if such a role exists, there are likely to be mechanoregulatory stimuli in cellular response through the depth of the reserve zone. A poroelastic multiscale finite element model of bone/growth-plate/bone was developed for examining the reserve zone cell transient response when compressed to 5% of the cartilage thickness at strain rates of 0.18%/s, 5%/s, 50%/s, and 200%/s. Chondrocyte maximum principal strains, height-, width-, and membrane-strains were found to be highly dependent on reserve zone tissue depth and strain rate. Cell-level strains and fluid transmembrane outflow from the cell were influenced by the permeability of the calcified cartilage between subchondral bone plate and reserve zone and by the applied strain rate. Cell strain levels in the lower reserve zone were less sensitive to epiphyseal permeability than in the upper reserve zone. In contrast, the intracellular fluid pressures were relatively uniform with reserve zone tissue depth and less sensitive to epiphyseal permeability. Fluid shear stress, induced by fluid flow over the cell surface, provided mechanoregulatory signals potentially sufficient to stimulate reserve zone chondrocytes near the subchondral bone plate interface. These results suggest that the strain rate and tissue depth dependence of cell-level strains and cell surface fluid shear stress may provide mechanoregulatory cues in the reserve zone.

**Keywords** Cartilage mechanics · Reserve zone chondrocyte deformation · Fluid flow shear stress · Mechanotransduction · Poroelastic · Biphasic

## 1 Introduction

Growth plate cartilage consists of two main components: interstitial fluid consisting of water with dissolved solutes and a solid matrix comprised mainly of collagen and proteoglycans (Mow et al. 1980). Previous studies on articular cartilage have shown that cartilage behaves as a biphasic material and deformation of the tissue induces fluid flow through the solid matrix (Mow et al. 1980, 1990). Due to

the high-water content of cartilage (~70%), the interstitial fluid plays a vital role in the tissue response to physiological loads (Lai et al. 1980). When cartilage is loaded at high strain rates with short time scales of the order of <200 ms, such as during heel strike phase in gait, the interstitial fluid becomes trapped and has insufficient time to flow through the pores. The tissue then behaves as an incompressible, single-phase elastic material (Eberhardt et al. 1990). Under conditions with longer time scales, fluid can flow through the tissue and the behavior becomes time-dependent, in which case poroelastic or biphasic theories can be employed. Both elastic models (Gao et al. 2014, 2015, 2017; Kazemi and Williams 2019; Leipzig et al. 2008; Nguyen et al. 2010; Sylvestre et al. 2007) and poroelastic computational models (Cohen et al. 1994, 1998; Komeili et al. 2020; Lacroix et al. 2002; Sergerie et al. 2009; Wu et al. 1997, 2000) have been developed to investigate the response of articular, growth plate, and fracture healing tissues to compression.

✉ Masumeh Kazemi  
mkzmmghd@memphis.edu  
John L. Williams  
jlwllm17@memphis.edu

<sup>1</sup> Department of Biomedical Engineering, University of Memphis, 330 Engineering Technology Building, Memphis, TN 38152, USA

Multiscale elastic models of the growth plate that include chondrocytes arranged in zonal distribution patterns have also been developed (Farzaneh et al. 2015; Gao et al. 2015, 2017; Kazemi and Williams 2019; Sergerie et al. 2009) to investigate the effects of forces applied across the growth plate on the mechanics at the cellular level.

Physiological loading modulates endochondral ossification and regulates cellular activity (Bries et al. 2012; Cancel et al. 2009; Carter et al. 1998; Frost 1990). The ability of chondrocytes to sense the mechanical environment is vital in the structural adaptation of cartilage to loading. Several mechanisms have been reported to explain signal transmission and consequent metabolic responses of chondrocytes. Cells may sense external stimuli by means of the stress–strain state produced at the cell boundary due to differences between matrix and cell mechanical properties. Cellular strains and fluid-flow-induced shear stress, imposed during tissue compression, act as mechanical stimuli through a variety of possible mechanisms including integrin receptors and stretch-activated ion channels (Guharay and Sachs 1984; Guilak and Mow 2000; Lacroix et al. 2002; Yellowley et al. 1997;). The pericellular matrix (PCM) may also serve as a possible signal transducer for cells (Alexopoulos et al. 2005; Kazemi and Williams 2019) in conjunction with the primary cilia. The primary cilium can act as an antenna on the cell surface to sense biomechanical and biochemical signals within the matrix (Seeger et al. 2012; Shao et al. 2012). In order to study the various mechanisms involved in the complex process of mechanical transduction, it is first necessary to precisely define the stress, strain, and fluid flow environments in the vicinity of the cartilage cell. A variety of studies have evaluated the mechanical properties and stress–strain distribution within growth plate cartilage either experimentally, using confined or unconfined compression (Cohen et al. 1994; Sergerie et al. 2009), tensile testing (Williams et al. 2001), nanoindentation (Radhakrishnan et al. 2004), image-based strain mapping (Wosu et al. 2012), or computational modeling (Cohen et al. 1998; Gao et al. 2015; Shefelbine and Carter 2004). Elastic models of growth plate cartilage have suggested that maximum principal strain, or distortional strain, and hydrostatic stress act as mechanoregulatory factors at the tissue level in the differentiation of cells to produce cartilage and bone (Carter and Wong 1988; Pauwels 1960). It has also been suggested that fluid-flow-induced shear stresses may provide biophysical stimuli to regulate tissue differentiation in bone fracture healing (Lacroix et al. 2002). Multiscale elastic models have shown that these principles also apply at the cell level for chondrocytes in the proliferative and hypertrophic zones (Gao et al. 2015, 2017) and reserve zone (Kazemi and Williams 2019) of the growth plate. However, these multiscale models did not consider the biphasic nature of the growth plate and cannot provide insight into any time-dependent and

fluid-related mechanoregulatory factors. Furthermore, while the biochemical and physiological function of the proliferative and hypertrophic zones has been extensively studied, the function of the reserve zone has long been unclear, as reserve zone cells appear to be in a quiescent state, but recent studies have shown that this zone contains a stem cell niche, which contributes cells to the columnar or proliferative zone and which we hypothesize may also contribute to subchondral bone plate formation in response to mechanoregulatory signals (Hallett et al. 2019; Kazemi and Williams 2018; Lui 2020; Matsushita et al. 2020). The subchondral bone plate is a zone that divides the articular cartilage from the epiphyseal spongy bone. Like the subchondral bone plate, the epiphyseal bone plate divides the cartilage from the epiphyseal spongy bone. Both bone plates are comprised of a calcified cartilage region adjacent to the unmineralized cartilage, and a layer of lamellar bone (Kazemi and Williams 2020). Some authors refer to the epiphyseal bone plate adjacent to the reserve zone as the ‘bone plate.’ Because of its histologic similarity to the subchondral bone plate underlying articular cartilage and because the name itself indicates as much, we refer to the bone plate supporting the growth cartilage as a subchondral bone plate.

The fluid flow boundary conditions at the two growth-plate chondro-osseous interfaces have been noted to be critical to the mechanical behavior of the cartilage (Cohen et al. 1994). By fitting computational biphasic model (Cohen et al. 1994) results to stress relaxation experiments, it was hypothesized that the interface of the epiphysis is more likely impermeable, while the large open marrow pores within the metaphysis are more permeable (Cohen et al. 1994). The relative permeability of articular and growth plate borders with bone was also investigated experimentally in an MRI study during simulated cyclic gait loading of sheep knee specimens (Song et al. 2013). The rate of consolidation and recovery of the articular cartilage was found to be slower than that of the growth plate cartilage, which was thought to be due to the open pore structure of the zone of provisional calcification and its border with metaphysis, whereas the dense subchondral bone plate underneath of articular cartilage limited the fluid exchange (Song et al. 2013). Beyond these studies, the question of the biomechanical effects of fluid exchange across the growth plate chondro-osseous junctions on the mechanical environment of chondrocytes in the growth plate remains unexplored, and more experimental and computational studies are required to address the fluid flow boundary conditions and their influence on tissue and cell response.

The main objective of this study was to develop a poroelastic multiscale finite element model of reserve zone cells within hydrated cartilage to characterize the stress–strain environments within and around reserve zone cells caused by the movement of interstitial fluid under pressure. We

believe that such a numerical approach can provide insight into the mechanotransduction events by which the mechanical microenvironment within and around chondrocytes and stem cells regulates cell differentiation and proliferation in the reserve zone. We hypothesized that fluid flow across the cell membrane, fluid-induced shear stress at the cell surface, cell membrane strains, and cell shape changes may provide mechanotransduction signals in reserve zone chondrocytes. We hypothesized that these mechanotransduction signals would be different in reserve zone cells near the subchondral bone plate than near the proliferative zone, and that their purported role in the process of organizing the growth plate into distinct zones of proliferation and hypertrophy during endochondral bone growth (Abad et al. 2002) would be related to these signals. To explore this, we investigated the influence of loading rate and of the reserve zone fluid boundary conditions on cell deformation. Such a numerical approach can enhance our understanding of the mechanical interactions between the cell and its surrounding matrix in zone of the growth plate.

## 2 Materials and methods

### 2.1 Global macroscale model description

An idealized axisymmetric multiscale finite element model of the physis representing a 5-mm-diameter cylindrical plug of bone/growth-plate-cartilage/bone was developed using Abaqus/CAE 2019 (SIMULIA, USA). The top and

bottom surfaces of the model were assumed frictionless, and impermeable (Fig. 1). The displacements normal to bottom surface and to the axis of symmetry were blocked while, on the other hand, the exterior edge parallel to the axis of symmetry was unconstrained and the pore pressure set to zero to simulate free draining along the exterior surface. The model was subjected to unconfined compression by applying a displacement to the top surface as a ramp function until it reached 0.025 mm or 5% of the overall growth plate cartilage thickness (0.5 mm) it was then held at that position until time = 1000 s, in order to simulate a stress relaxation test. The ramp loading was applied using strain rates of 0.18%/s, 5%/s, 50%/s, and 200%/s. The total reaction force at the base of the model was calculated as a function of time for comparison with experimental stress relaxation data.

The growth plate was modeled as being flat and oriented perpendicularly to the axis of symmetry of the specimen. The macroscale model included epiphyseal bone (EP), subchondral bone plate (SB), calcified cartilage (CC), growth plate reserve zone (RZ), growth plate proliferative/hypertrophic zone (PZ/HZ), provisional calcification (PC), and metaphyseal bone (MP). The thickness of the zones and the thickness ratio of reserve zone to the proliferative and hypertrophic zones in our model represent the average value of several histology sections across the growth plate of the femoral head of 480-day-old pigs. The cell/matrix volume ratio for the reserve zone is about 0.1 and this may affect the composite tissue level modulus. Rather than using a value for the ECM modulus and accounting for the cell/matrix

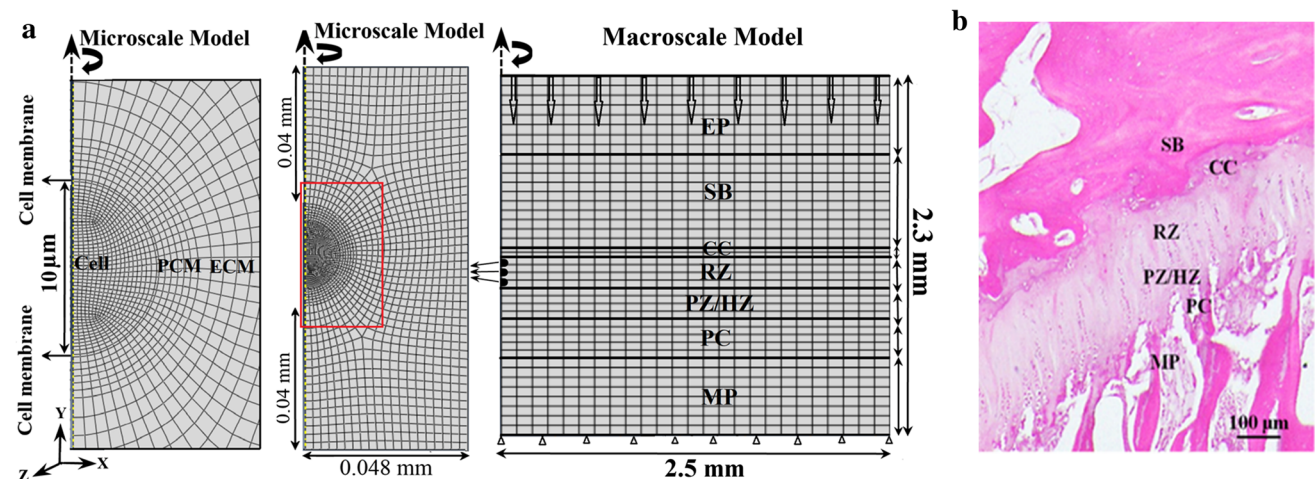


**Fig. 1** **a** The idealized axisymmetric poroelastic model shows tissue (macroscale) and cell (microscale) levels for cells positioned at three locations within the RZ. The tissue was subjected to a displacement of 5% of the cartilage thickness parallel to the axis of axisymmetry. It is restrained at the bottom (in the y-direction) and fluid is free to drain laterally. It includes the epiphysis (EP), subchondral bone plate (SB), calcified cartilage (CC), growth plate cartilage (reserve zone

(RZ), and proliferative/hypertrophic zone (PZ/HZ)), provisional calcification (PC), and metaphysis (MP). The macroscale model consists of three chondrons embedded in the extracellular matrix (ECM (RZ)). All chondrons are composed of chondrocyte cells surrounded by a thin cell membrane and enveloped by a pericellular matrix (PCM), **b** Histology image (stained with H&E) of a 480-day-old pig showing the histological regions used in macroscale model

volume, we used stress relaxation experiments to extract a homogenized modulus for the reserve zone including ECM and cells (Gao et al. 2014). The elastic modulus for the reserve zone was determined by optimizing the fit of simulations of a macroscale model of the growth plate (containing the reserve, proliferative and hypertrophic zones) to compression experiments. The modulus of the reserve zone was taken to be approximately twice that of the PZ/HZ zones as shown by Sergerie et al. (2009). All layers were considered to be poroelastic materials with fluid phase and homogeneous solid phase. In the

implementation in Abaqus, it was assumed that the fluid and solid phases were incompressible. All tissues were assigned linear elastic isotropic material properties and isotropic permeability values (Tables 1 and 2). To account for large deformation, the effect of geometrical nonlinearity NLGEOM was activated in Abaqus and finite element strains are reported as logarithmic strains. The macroscale mesh of elements with an element edge length of approximately 55  $\mu\text{m}$  was based on previous models for which convergence studies were performed (Gao et al. 2014, 2015, 2017). The total number of elements in the

**Table 1** Material properties of different layers in the macroscale model

Tissue	E (MPa)	$\nu$	$K_0$ ( $\text{mm}^4/\text{N.s}$ )	$e_0$	$M$ (dimensionless)	Thickness (mm)*
Subchondral bone plate (SB)	2000 <sup>a</sup>	0.2 <sup>a</sup>	90 <sup>b</sup>	0.176 <sup>a</sup>	–	0.6
Calcified cartilage (CC)	300	0.2 <sup>c</sup>	90 <sup>d</sup>	1.1 <sup>d</sup>	–	0.06
Reserve zone (RZ)	0.98 <sup>e</sup>	0.125 <sup>f</sup>	$1.41 \times 10^{-3}$ <sup>g</sup>	4.25 <sup>f</sup>	5.48 <sup>d</sup>	0.25
Proliferative/hypertrophic zone (PZ/HZ)	0.49 <sup>e</sup>	0.125 <sup>f</sup>	$5.8 \times 10^{-3}$ <sup>g</sup>	3.6 <sup>f</sup>	6.435 <sup>**d</sup>	0.25
Provisional calcification (PC)	100	0.2	$22.5 \times 10^{-5}$ <sup>***</sup>	3.5 <sup>****</sup>	–	0.15
Epiphysis (EP)	1000	0.2	$45.3 \times 10^5$ <sup>b</sup>	3.7 <sup>d</sup>	–	0.5
Metaphysis (MP)	1000	0.2	$45.3 \times 10^5$ <sup>b</sup>	3.7 <sup>d</sup>	–	0.5

\*Based on our histology of growth plate for a 480-day-old pig proximal femur (Kazemi and Williams 2020). The harvesting of tissue was exempt from IACUC review as it was obtained from euthanized animals in another University of Memphis IACUC approved study

\*\*This value was obtained by averaging values of the middle zone and deep zone of articular cartilage tissue

\*\*\*This value is assumed to be half of the EP/MP permeability

\*\*\*\*A value close to that of the HZ

<sup>a</sup>From Moo et al. 2014, articular cartilage

<sup>b</sup>From Hwang et al. 2008, human knee articular cartilage

<sup>c</sup>From Fan et al. 2009, rat tibia articular cartilage

<sup>d</sup>From Stender et al. 2017, articular cartilage

<sup>e</sup>From Gao et al. 2015, yearling bovine tibia growth plate

<sup>f</sup>From Sakai et al. 2015, porcine knee articular cartilage

<sup>g</sup>From Sergerie et al 2009, newborn distal ulna porcine growth plate

**Table 2** Material properties used for microscale model

Region	E (MPa)	$\nu$	$k_0$ ( $\text{mm}^4/\text{N.s}$ )	$e_0$	$M$ (dimensionless)*	Radius, R/ Thickness, T( $\mu\text{m}$ )
Cell	0.002 <sup>a</sup>	0.04 <sup>b</sup>	$4.2 \times 10^{-3}$ <sup>c</sup>	4.88 <sup>c</sup>	5.48	R 5 <sup>d</sup>
Cell membrane	$4 \times 10^{-2}$ <sup>c</sup>	0.04 <sup>b</sup>	$3 \times 10^{-9}$ <sup>c</sup>	3 <sup>c</sup>	5.48	T 0.1 <sup>e</sup>
Pericellular matrix (PCM)	0.265 <sup>a</sup>	0.04 <sup>b</sup>	$4 \times 10^{-5}$ <sup>f</sup>	4 <sup>f</sup>	5.48	T 0.5 <sup>d</sup>

\*The same value that was used for ECM (RZ) in the macroscale model Moo et al. (2014)

<sup>a</sup>From Gao et al. (2015)

<sup>b</sup>From Alexopoulos et al. (2005)

<sup>c</sup>From Moo et al. (2014)

<sup>d</sup>From Kazemi and Williams (2019)

<sup>e</sup>From Moo et al. (2012)

<sup>f</sup>From Wu and Herzog (2000)

global model was 11,903. The permeability of growth plate cartilage zones (RZ and PZ/HZ) was assumed to be strain-dependent, while it was assumed to be constant within the less deformable bone and calcified cartilage regions in the model. The CC is a thin layer of calcified cartilage between reserve zone and subchondral bone plate, while the PC layer is the zone of provisional calcification; this is a calcified layer between hypertrophic zone and metaphysis where the mineralized cartilage “bars” transition into the primary spongiosa. This layer has greater porosity than the CC layer and is therefore assumed to have higher permeability to fluid flow. The strain-dependent hydraulic permeability, or mobility ( $\text{mm}^4/\text{N}\cdot\text{s}$ ), was defined in terms of the void ratio and current strain by Eq. 1 (Ficklin et al. 2009; Lai and Mow 1980) and was utilized to define the permeabilities of the RZ and PZ/HZ in the macroscale model and of the cell, cell membrane, and PCM in the microscale model.

$$k = k_0 \left[ \frac{e}{e_0} \right]^2 \exp \left( \frac{M}{2} \left( \left( \frac{1+e}{1+e_0} \right)^2 - 1 \right) \right), \quad (1)$$

where  $k_0$  refers to the initial hydraulic permeability at zero strain ( $\text{mm}^4/\text{N}\cdot\text{s}$ ),  $e_0$  and  $e$  are initial and current void ratios and  $M$  is a non-dimensional constant that accounts for the additional compaction of the cartilage due to diffusive drag causing a nonuniform and nonlinear decrease in permeability with increasing strain of the tissue (Lai and Mow 1980, 1981; Ficklin et al. 2009). The initial void ratio was defined by the volume fraction of fluid divided by the volume fraction of solid at 0% strain. The current void ratio,  $e$ , can be measured from the applied strain ( $\epsilon$ ) by the relationship (Sakai et al. 2015):

$$\epsilon = (e - e_0) / (1 + e_0) \quad (2)$$

We provided the permeability values as used in the Abaqus program (Eq. 3) by means of a user-defined lookup table that lists the Abaqus definition of hydraulic conductivity ( $\dot{K}$ ,  $\text{mm}/\text{s}$ ) values as a function of the void ratio which were obtained by multiplying the hydraulic permeability ( $\text{mm}^4/\text{N}\cdot\text{s}$ ) calculated from Eq. (1) (Mow et al. 1980) by the specific weight ( $\text{N}/\text{mm}^3$ ) of the wetting fluid ( $\gamma_f = 9.81 \times 10^{-6} \text{ N}/\text{mm}^3$ ) assumed to be water at body temperature (Stender et al. 2017). All layers were assumed to be initially fully saturated with fluid.

$$\dot{K} = k \cdot \gamma_f \quad (3)$$

The hydraulic permeability for the marrow spaces in cancellous bone of the metaphysis and epiphysis was estimated by dividing values of bone permeability published in units of  $\text{length}^2$  (Grimm and Williams 1997; Nauman

et al. 1999) by the dynamic (absolute) viscosity of water (defined as  $10^{-3} \text{ Pa}\cdot\text{s}$ ).

## 2.2 Microscale submodel model description

The submodel function within Abaqus was used to transfer displacements, reaction forces, and pore pressures from the global model as boundary conditions for the microscale submodels (Fig. 1). Microscale submodels were created for three poroelastic chondrocytes surrounded by a thin cell membrane and wrapped with a narrow region of pericellular matrix (Poole et al. 1987), all embedded within the reserve zone. Cells were assumed to be perfectly bonded to the matrix. A normalized tissue depth,  $\xi$ , was defined as measured vertically from the RZ-CC border where  $\xi=0$  to the RZ-PZ border where  $\xi=1$ . Cell 1 (closest to CC border) is located at  $\xi=0.08$ , cell 2 (in the middle of RZ) is embedded in  $\xi=0.48$ , and cell 3 (closest to PZ/HZ border) is at  $\xi=0.84$ . To represent the poroelastic nature of the cartilage tissue and chondrocytes, a four-node bilinear displacement and pore pressure element (CAX4P) was used. A mesh refinement study was performed by increasing the number of elements in the cell region until the maximum principal strains and fluid velocities in the cells became independent of the mesh resolution, which occurred when the number of elements inside the cell reached 300 with edge lengths of  $0.13 \mu\text{m}$  or less. The material properties for the microscale model are listed in Table 2.

To study the effect of the permeability boundary conditions at the calcified cartilage interfaces on the transient response of the cell and fluid flow across the cell membrane, a second model was developed in which the hydraulic permeability of the CC ( $k_0=90 \text{ mm}^4/\text{N}\cdot\text{s}$ ) was replaced with very low permeability value ( $k_0=5.8 \times 10^{-3} \text{ mm}^4/\text{N}\cdot\text{s}$ ) equal to that of the PZ, to represent a nearly impermeable interface with the reserve zone.

Cell-averaged maximum tensile principal strain, cell height, cell width strain (Kazemi and Williams 2019), and cell membrane strain were calculated for all cases. Cell height and width strains were calculated from the change in the cell horizontal diameter and vertical radius, respectively, with respect to the pre-compression values. The fluid-flow-induced shear stress was calculated at three locations on the cell surface (0 (cell north pole), 90 (cell equator), and 180 (cell south pole) degrees) by  $\tau = \mu dv/dn$  in which  $\mu$  is the dynamic fluid viscosity, defined as  $10^{-3} \text{ Pa}\cdot\text{s}$ , and  $dv/dn$  is the surface fluid velocity gradient perpendicular to the cell surface as determined by evaluating the adjacent element nodal values in the pericellular matrix (Gupta et al. 2006; Lavagnino et al. 2008). All the results were extracted at 95% of the peak applied displacement (4.5% nominal strain across the growth plate cartilage) to avoid any possible numerical artifact that may result from sudden zero

acceleration at the peak applied load (5% strain) in the ramp function. For convenience, we will refer to nominal applied strain of 5% rather than the 4.5% strain at which the data were extracted. The data were extracted at  $t=25, 0.9, 0.09,$  and  $0.0225$  s for 0.18%/s, 5%/s, 50%/s, and 200%/s, respectively, corresponding to the times required to reach 4.5% strain. Unless otherwise noted strains are reported as logarithmic strains, while applied strains are given as nominal (engineering) strains.

### 3 Results

Depth-dependent maximum principal strains and intracellular fluid pressures are shown in line graphs, grouped by cell location within the RZ for all the applied strain rates (Fig. 2a).

#### 3.1 Intracellular maximum principal strain

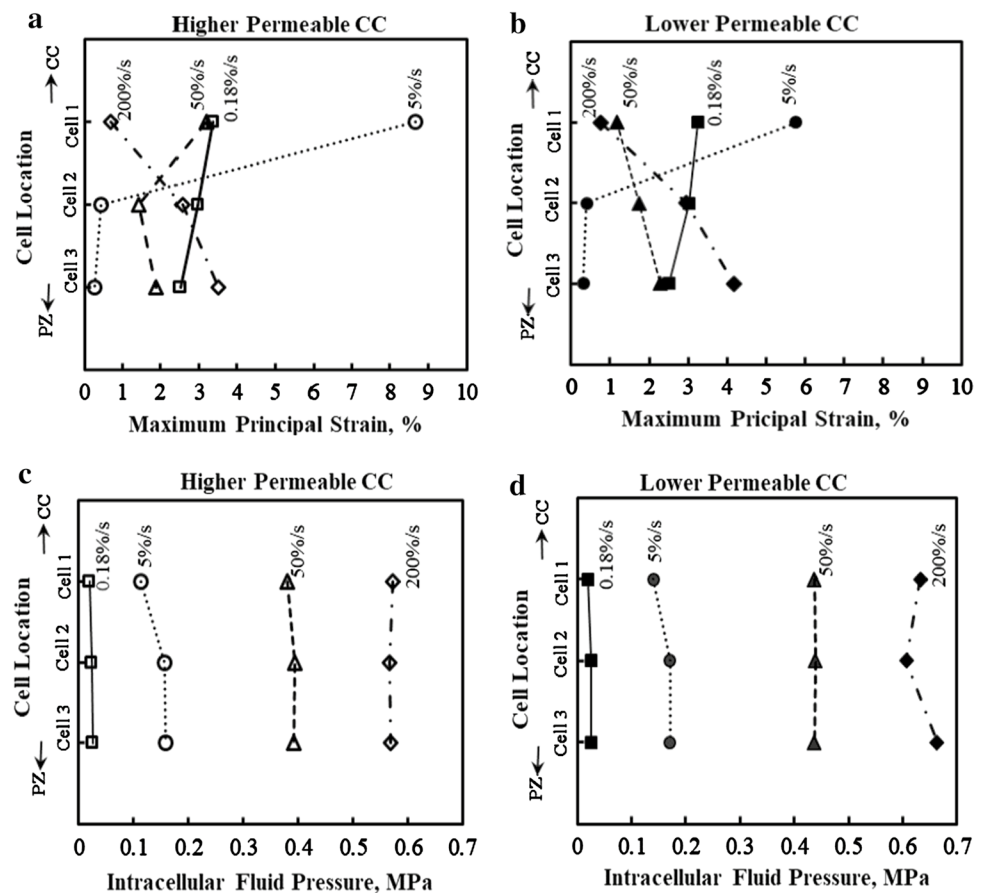
For the three lowest strain rates (0.18%/s, 5%/s, and 50%/s), the maximum principal strain in the cell decreased from the calcified cartilage (CC) border ( $\xi=0.08$ ) to the proliferative/hypertrophic (PZ/HZ) interface ( $\xi=0.84$ ). The

highest magnitude of maximum principal strain (9%) was experienced at an applied strain rate at 5%/s by the cell nearest to the CC border, representing a twofold amplification of applied tissue strain. In contrast, at a loading rate of 200%/s, the maximum principal strain magnitude in the cell increased from the CC border to the PZ/HZ interface. This reversal in the pattern with cell location can be seen to already begin at a strain rate of 5% between cell locations in the middle of the reserve zone and the cell close to the proliferative zone (Fig. 2a). Decreasing the permeability of the CC decreased all the strain values but did not change the overall cellular strain pattern (Fig. 2b). Restricting fluid transfer across the CC caused the maximum principal strains in the cell closest to the CC to decrease by nearly 33% and 63% at 5%/s and 50%/s, respectively (Fig. 2b), whereas it increased slightly (20%) for the cell near the PZ/HZ at 50%/s and 200%/s.

#### 3.2 Intracellular fluid pressure

Figure 2c,d represents the intracellular fluid pressure for the conditions of a higher permeable and lower permeable CC. Intracellular fluid pressures increased with the applied strain rate. At each individual strain rate, there were no significant

**Fig. 2** Comparison of maximum principal strains (logarithmic strains) and intracellular fluid pressures with higher permeable (a&c) and lower permeable calcified cartilage properties (b,d) at the 4.5% strain time point and 0.18%/s, 5%/s, 50%/s, and 200%/s strain rates for three cells, Cell 1 (close to CC border), Cell 2 (in the middle of the RZ), Cell 3 (close to PZ border), embedded in the reserve zone (RZ). CC = Calcified Cartilage, PZ = Proliferative Zone



differences in intracellular fluid pressure for cells at different locations (Fig. 2c). The smallest magnitude in pressure of 0.02 MPa occurred at the slowest loading rate of 0.18%/s when fluid had time to flow and the interstitial fluid pressure had dissipated. Reducing fluid exchange across the CC due to decreased permeability caused a slight increase intracellular fluid pressures in all locations (Fig. 2d). For the cell closest to CC border, lower permeability at the CC border increased the intracellular pressure by 23% at 5%/s and 15% at 50%/s.

### 3.3 Cell height and width strain

The magnitudes of cellular height and width strains followed a similar trend with cell location as did maximum principal strains (Fig. 3a, c). The positive values of cellular width strain and negative values of height strain indicate that cells flattened under the applied compression (Fig. 3a, c). The width strain values closely matched those of maximum principal strains at each equivalent cell location and strain rate, indicating that the maximum principal strains acted across the width of the cells and were highly location dependent. Restricting fluid from crossing the CC decreased the cell

height change by 27% and increased the width change by 30%, respectively, at the 5%/s strain rate for the cell nearest the CC border and caused slight increases in the cell width and height changes for the cell close to the PZ at 50%/s (21% for both height and width) and 200%/s (16% for both height and width) (Fig. 3b,d).

### 3.4 Fluid velocity across the cell membrane

As can be seen for the cell close to the CC in Fig. 4, the resultant fluid velocity vectors across the cell membrane are not distributed uniformly around the cell periphery. For permeable boundary conditions at the CC/RZ interface, the maximum fluid velocity values are found at the top surface toward the subchondral bone plate (0 degree) at all applied strain rates (Fig. 4a). As with cell-level strains, the maximum magnitudes of the fluid velocity occurred at 5%/s and the lowest at 200%/s. Lower permeable boundary conditions at the CC/RZ interface caused the fluid velocity across the cell membrane to decrease in all cases (Fig. 4). While a lower permeable CC did not affect the direction of fluid flow at the three lowest strain rates (0.18%/s, 5%/s, and 50%/s), it did cause a reversal in the direction of fluid flow across the cell membrane at the highest strain rate of 200%/s (Fig. 4,

**Fig. 3** Depth-dependent cellular height- (a,b) and width- (c&d) strains with higher permeable (a,c) and with lower permeable calcified cartilage properties (b&d) at 4.5% strain for 0.18%/s, 5%/s, 50%/s, and 200%/s strain rates for Cell 1 (close to CC border), Cell 2 (in the middle of the RZ), Cell 3 (close to PZ border), embedded in the reserve zone (RZ). CC= Calcified Cartilage, PZ=Proliferative Zone

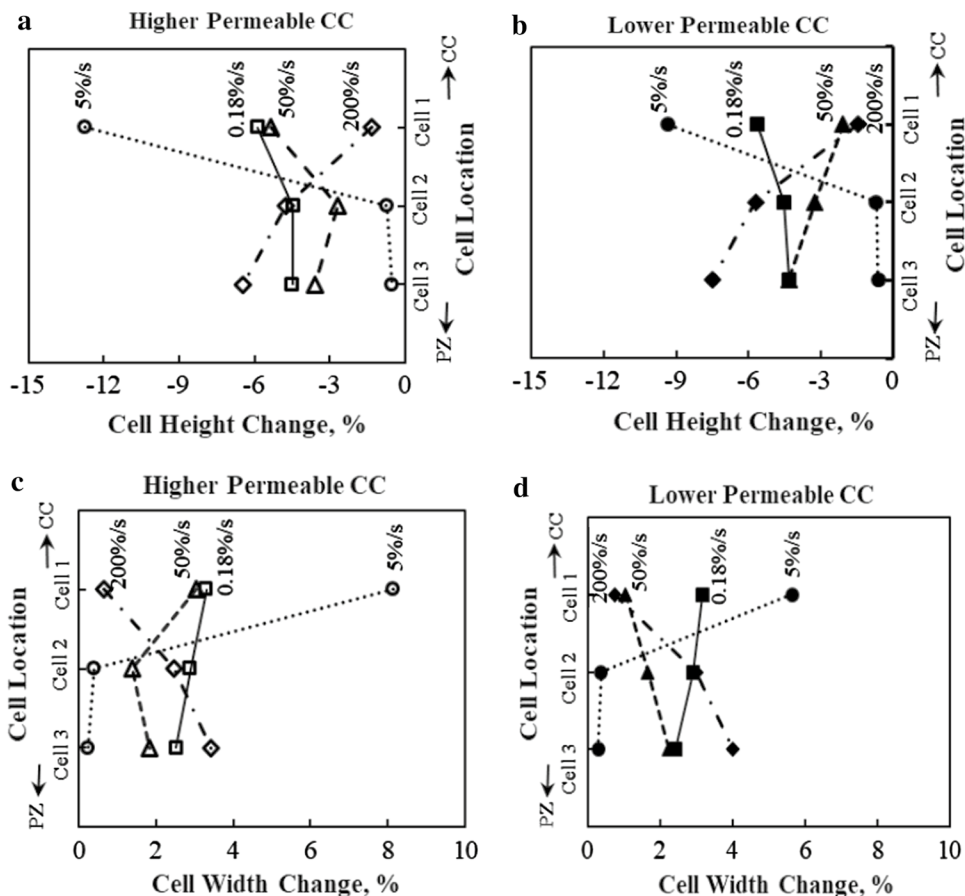
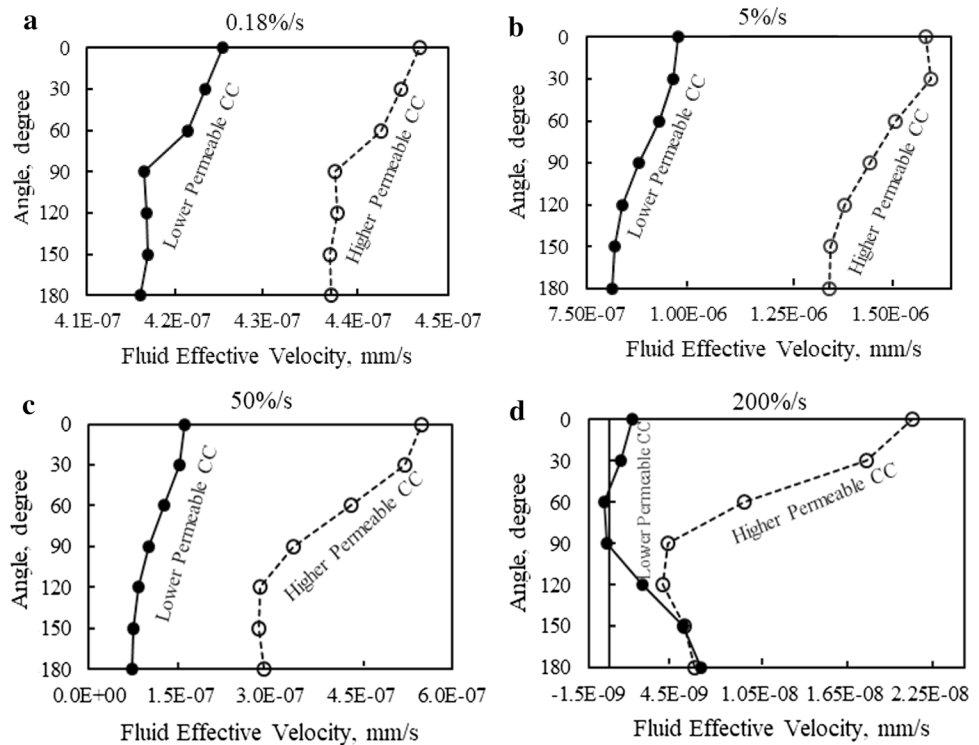


**Fig. 4** The fluid transmembrane outflow velocity (mm/s) for the cell close to CC border at 4.5% applied strain for higher and lower permeable CC, **a** at 0.18%/s, **b** at 5%/s, **c** at 50%/s, and **d** at 200%/s strain rates, 0 degrees is at the cell north pole facing the CC/SB border, 90 degrees is at the cell equator and 180 degree is at the cell south pole facing the PZ border



between 60 and 90 degrees) such that fluid flowed into the cell over much of the top half and out of the bottom half in contrast to what happened when the CC was permeable and the fluid mainly flowed out of the top of the cell (Fig. 4d).

Lower CC permeability also tended to change the pattern of flow direction within the cell as well (relative plots not included) as across the cell membrane for the 200%/s strain rate due to the increased resistance to flow across the CC border. For a higher permeable CC, the peak values of transmembrane fluid velocities were  $0.45 \times 10^{-6}$ ,  $1.63 \times 10^{-6}$ ,  $0.55 \times 10^{-6}$ , and  $0.02 \times 10^{-6}$  mm/s at the strain rates of 0.18%/s, 5%/s, 50%/s, and 200%/s, respectively. For a lower permeable CC, the corresponding peak transmembrane fluid velocities were  $0.43 \times 10^{-6}$ ,  $0.98 \times 10^{-6}$ ,  $0.16 \times 10^{-6}$ , and  $0.006 \times 10^{-6}$  mm/s.

### 3.5 Cell membrane strain

Our microscale model predicted that the maximum tensile strain in the cell membrane (logarithmic strains in the x-direction) occurred at the top and bottom of the cells, where these were acting tangentially along the membrane. For the cell located near the CC, it was generally much higher at 5%/s than at other strain rates. This strain component followed a similar trend with location to what was reported for width and height strain at all strain rates (Fig. 5a). For the cell near the CC, imposing nearly impermeable conditions in the CC/RZ interface had the smallest

effect at the slowest and highest strain rates (Fig. 5b). However, it caused the tangential membrane strain to decrease by about 26.5% at 5%/s and 66.5% at 50%/s for the cell closest to the lower permeable CC border.

### 3.6 Fluid-flow-induced shear stress at the cell membrane surface

The magnitude of fluid-flow-induced shear stress varied with position along the surface of the cell and with cell location as a function of tissue depth within the RZ. Shear stress values are presented only for the higher permeable CC boundary conditions (Fig. 6). For the cell close to the CC border, strain rate had a profound effect on the localized shear stress at the cell surface, increasing in magnitude with strain rate, with the greatest stress magnitude at occurring at 200%/s (Fig. 6). At this location in the reserve zone cell surface fluid shear stresses were greater at the cell equator (90-degree angle) compared to the north and south poles (0 and 180 degrees), respectively (Fig. 6c). The fluid-induced shear stresses were much lower at locations further from the CC.

## 4 Discussion

In this study, a multiscale poroelastic model was developed to investigate the compressive behavior of the cell at various depths within the reserve zone (RZ) of the growth plate and at different strain rates using a poroelastic finite element



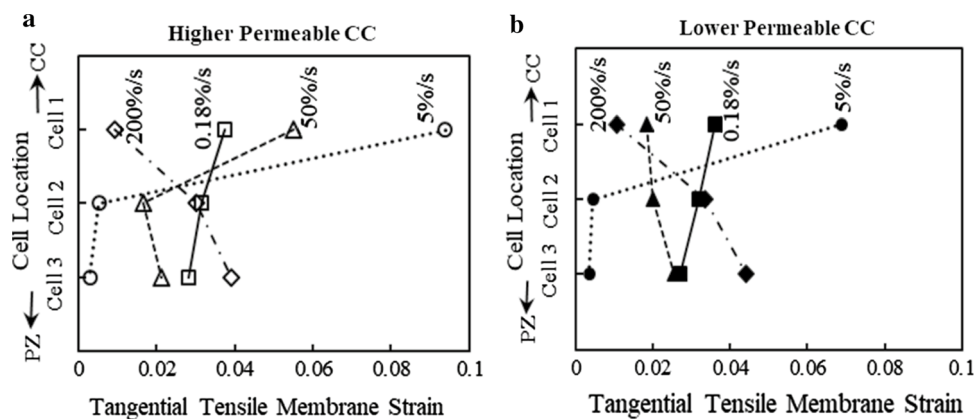


**Fig. 5** Peak tangential tensile membrane strains for cells located at the calcified cartilage border, middle of the reserve zone, and close to proliferative/hypertrophic zone border subjected to 5% strain at four different strain rates assuming higher permeable **a** and lower perme-

able **b** calcified cartilage properties for Cell 1 (close to CC border), Cell 2 (in the middle of the RZ), Cell 3 (close to PZ border), embedded in the reserve zone (RZ). CC=Calcified Cartilage, PZ=Proliferative Zone

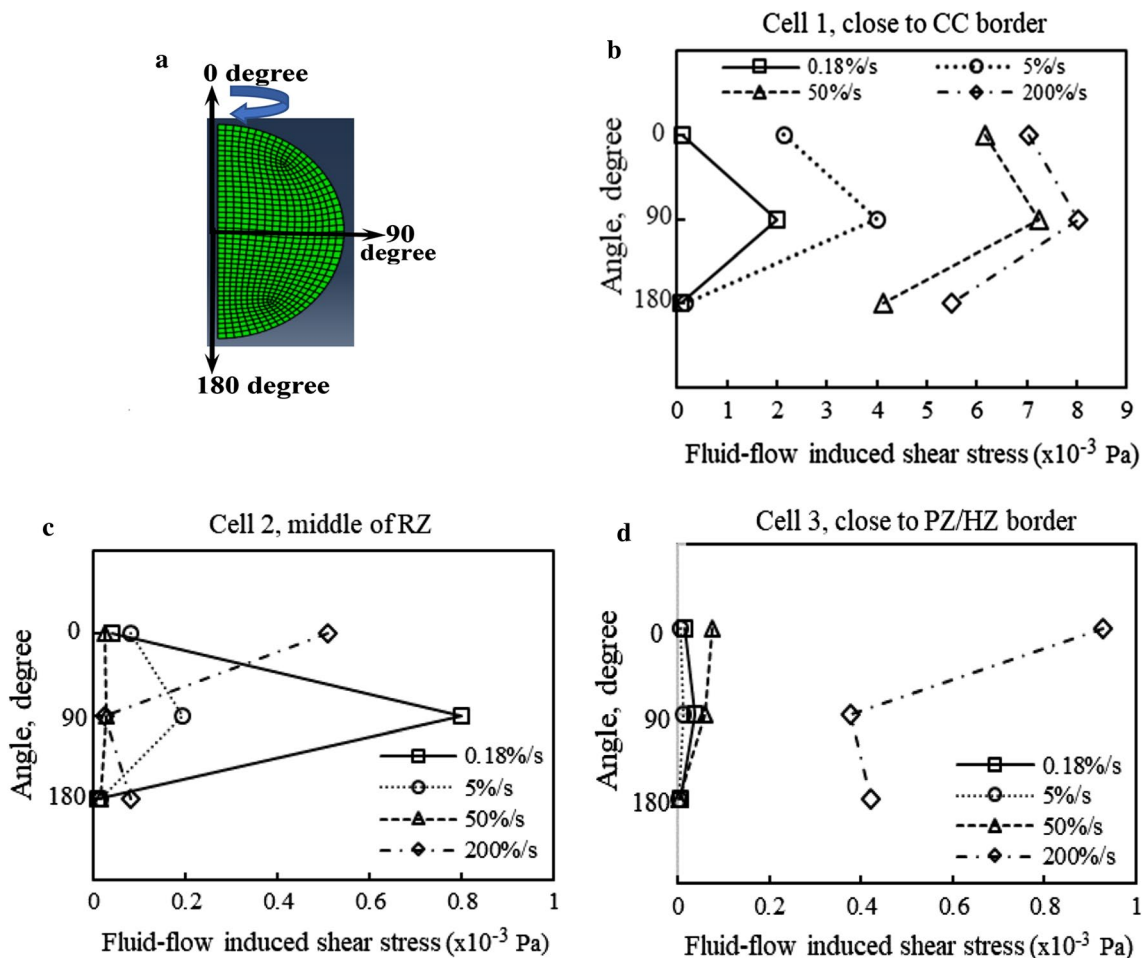


**Fig. 6** The peak values of depth-dependent fluid flow shear stress ( $\times 10^{-3}$  Pa) at **a** the cell surface for three angles of 0, 90, and 180 degrees, for **b** the cell close to calcified cartilage border, **c** the cell in the middle of the RZ and **d** the cell close to the PZ border at 4.5%

strain for four different strain rates with permeable calcified cartilage properties. Shear stress values above  $0.4 \times 10^{-3}$  may have physiological relevance

modeling framework. The model consists of 0.5 mm layers of cancellous bone on either side of the 0.5 mm thick growth cartilage and includes the subchondral bone plate with a layer of calcified cartilage between the plate and the cartilage. Linear elastic properties were assumed for the solid structures and the permeability of growth plate cartilage was assumed to be strain-dependent, while it was assumed to be constant for all the other parts of the model. Loading was applied by means of a ramp displacement function at four different strain rates until a nominal strain of 5% across the growth plate cartilage. Results are compared at an applied strain level of 4.5% during ramp loading to 5% strain overall, but the time required to reach maximum applied nominal strain varies with loading rate and this affects the time available for fluid to move through tissues and across interfaces of between tissues with different permeabilities. The results may be more easily interpreted in terms of the approximate time durations over which the ramp loading was applied, 25 s, 0.9 s, 0.09 s, and 0.0225 s.

#### 4.1 Depth-dependent pattern of cell strains and cell membrane strain

The results of the study revealed that all the cell strain magnitudes (maximum principal strain, cell width and height strains, and peak tangential membrane strains) were highly dependent on the depth of the cell within the RZ and the rate of loading. The effects of increasing loading rates on cellular strains presented a complex pattern. At the three slower rates of loading, strain measures decreased with depth for a given loading rate as the cell location within the RZ moved from the CC to the proliferative zone (PZ). This decrease was gradual for 0.18%/s, but a drastic decrease was observed for the 5%/s rate between the cell near the CC and the cell in the middle of the RZ (Figs. 2a,b 3). At the third higher loading rate of 50%/s, all the strain measures decreased from the CC to the middle before increasing slightly near the PZ. At the fastest loading rate, a reverse pattern was observed in which all the strain measures increased steadily with tissue depth within the reserve zone. This pattern may be explained by considering the internal cell pressure, the velocity of the fluid exuded from the cell, and the fluid velocity across the CC and PZ borders of the reserve zone. Fluid velocities in the reserve zone ECM region around the cell located at the CC border increased with strain rate between 0.18%/s and 50%/s, all directed toward the CC border. The velocity through the PCM was directed around the cell and toward the CC interface. At the fastest loading rate of 200%/s, corresponding to impact loading, the fluid velocity in the ECM and within the PCM around this cell flowed in the direction of the CC border around the top half of the cell and toward the PZ border around the bottom half of the cell. These results may be explained by considering the relative

permeabilities at the two interfaces and the proximity of the cell to the CC interface which is 15,500 times more permeable than the PZ interface.

Fluid flow has a significant influence on cell deformation. The highest cellular strain of the cell close to CC occur at 5%/s and coincides with the higher fluid flow out of the cell (Fig. 4). Transmembrane fluid velocities increase when the intracellular fluid pressure exceeds that in the matrix (Accadbled et al. 2008; Soltz and Ateshian 1998). The close proximity of the first cell (Cell 1) to the comparatively much more permeable CC/SB layer allows fluid around this cell to readily flow into the CC, thereby decreasing the pericellular fluid pressure and amplifying cell-level strains to twice the applied strain at a 5%/s strain rate. Transmembrane fluid outflow velocities are greater at the cell north pole than anywhere else around the cell circumference (Fig. 4). At a 5%/s loading rate, the differences in fluid pressures inside and outside Cell 1 and the proximity to the permeable CC border are sufficient to drive fluid out of the cell during the 0.9 s time period of ramp loading. The intra-extra-cellular fluid pressure differential decreases for cells located further from the reserve zone borders. At the slowest strain rate of 0.18%/s, there is adequate time (25 s during ramp loading) for ECM fluid pressures to dissipate. Cell strain levels decrease with distance from the CC layer at the two lower strain rates due to the lower permeability of the PZ interface, which decreases the pressure differential between the cell and surrounding matrix. At the two faster loading rates, there is insufficient time (0.09 s for 50%/s and 0.0225 s for 200%/s) for the fluid to exit the cell or leave the reserve zone resulting in larger ECM fluid pressures around the cell and reducing transmembrane fluid outflow velocities, as well as the cell-level strains. At 50%/s conditions approach the behavior of a single-phase material since the fluid is becoming trapped between the two reserve zone boundaries and within the cell. At 50%/s, cell strains decrease with distance from the CC and then increase as the PZ is approached. At this strain rate, the purely elastic properties are beginning to dominate the response. Under impact loading at 200%/s, we observe a depth-dependent cell-level strain profile that resembles what was reported for a purely elastic solution (Kazemi and Williams 2019), where the cell strains increase steadily with distance from the CC border as the cell approaches the PZ, which has half the elastic modulus of the reserve zone. The lower CC permeable boundary condition at the rapid impact of 200%/s increases the resistance to fluid exchange through the chondro-osseous junction and increases the ECM fluid pressure outside the cell, which reduces the maximum tensile strain and cell width strains in comparison with these cell strains for a more permeable CC condition.

At the faster strain rate, the highest tangential strain in the cell membrane occurred at the north and south poles (top and bottom) of the cell, which may be possible locations of

cell damage under high impact loading. Membrane stretch may be a possible mechanism for mechanical signal transduction by activating ion channels (Guharay and Sachs 1984; Morris and Sigurdson 1989). It has been suggested that the tangential membrane strain may have a role in chondrocyte death during high strain rate compression (Moo et al. 2012) as short bouts of impulsive strain rates can lead to cell damage (Argote et al. 2019; Moo et al. 2012; Morris and Sigurdson 1989).

#### 4.2 Depth-dependent intracellular fluid pressure and the influence of CC permeability

Intracellular fluid pressure was found to be relatively independent of the depth of the cell within the RZ layer and of CC permeability, increasing only slightly as the CC permeability was reduced (Fig. 2c,d). Intracellular fluid pressures increased 30-fold as strain rates increased, rising from 0.02 MPa at 0.18%/s to about 0.58 MPa at 200%/s. This increase in intracellular fluid pressure was considerably less than the 1000-fold increase in loading rate, suggesting that cells are protected from experiencing large increases in intracellular fluid pressure at high strain rates. These values are in the range of extracellular pore pressures (0.2–0.6 MPa) reported for simulated unconfined compression of articular cartilage plugs to 10% at 0.17%/s (Pérez and Doblaré 2006) and for intracellular fluid pressure for chondrocytes within articular cartilage plugs under 15% imposed strains (Wu and Herzog 2000). The smallest intracellular fluid pressure occurs at the slowest strain rate and is associated with the escape of fluid from the cell as more time is allowed during the slower loading rate which results in fluid pressure dissipation. Conversely, the higher fluid pressure at rapid compression relates to the fluid resistance due to the negligible

fluid drainage out of the cell over a very short time (Argote et al. 2019). Similar observations were made for articular cartilage subjected to confined compression of 5% strain, in which cartilage was modeled as a hyperplastic inhomogeneous material (Moo et al. 2012).

The strain rate affects the percentage of load-bearing supported by fluid and solid phases. With a higher strain rate, the contribution of fluid for load-bearing increases (Argote et al. 2019; Pérez and Doblaré 2006). At the tissue level, the extracellular fluid pore pressure within the cartilage is associated with the load-bearing of the joint and it can support up to 95% of the applied load, while the remaining load is supported by collagen and proteoglycan of the cartilage matrix (Soltz and Ateshian 1998). This effectively increases the apparent modulus of the hydrated tissue at higher loading rates (Fig. 7a). The modulus of the stress–strain curve in Fig. 7a for the strain rate of 0.18%/s is equivalent to the experimentally obtained modulus for yearling calf growth plates tested in compression at the same strain rate (Tutorino et al. 2012).

The intracellular pressures at 4.5% strain shown in Fig. 2 are less than or equal to the applied stress levels in Fig. 7a for the two lowest strain rates and slightly exceed the applied stress at the two higher strain rates: 0.02 vs 0.03 MPa at 0.18%/s; 0.12 vs 0.12 MPa at 5%/s; 0.38 vs 0.25 MPa at 50%/s; 0.58 vs 0.35 MPa at 200%/s (values for the more permeable CC). The intracellular pressures do not rise in direct proportion to strain rate. This can be explained by considering the 64,000-fold greater permeability of the CC and SB compared with the ECM and the 13,000-fold greater permeability of the PCM relative to the cell membrane. Tissue and intracellular fluid pressures rise with increased rate of loading as there is insufficient time for the fluid to exit the tissue despite increased

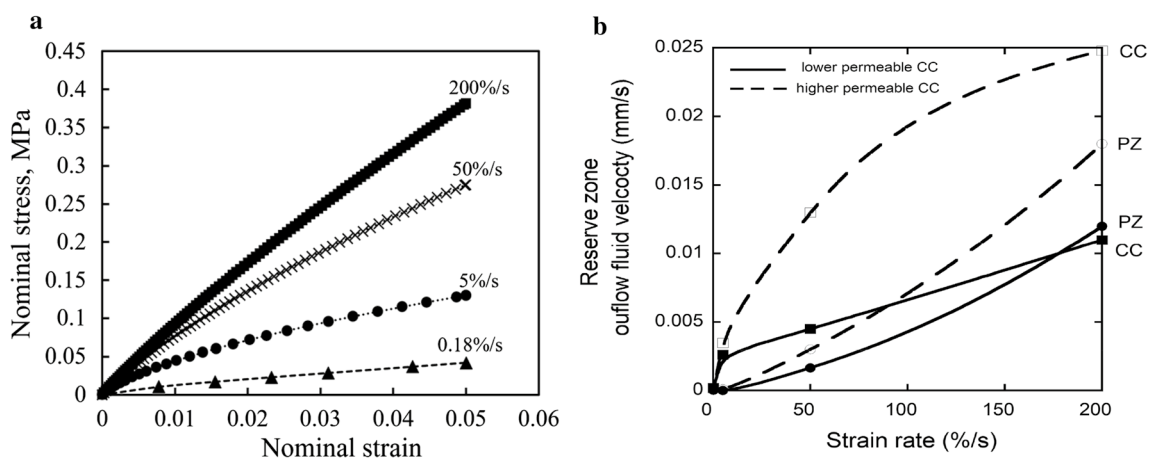


**Fig. 7** a Calculated nominal stress as a function of nominal strain during the ramp phase of loading to a 5% nominal strain, **b** Interstitial fluid outflow velocity across the CC and PZ interfaces as a func-

tion of strain rate for higher and lower permeable CC conditions. The direction of flow is toward the epiphysis at the CC border and toward the metaphysis at the PZ border

outflow velocities across the RZ borders (Fig. 7b). Outflow occurs across both the CC and PZ borders to allow fluid pressure levels to remain approximately uniform through the depth of the reserve zone.

### 4.3 Depth-dependent transmembrane fluid velocity and the influence of CC permeability

The cellular strains were affected by the boundary constraints and fluid flow across the tissue. A nominal strain rate of 0.18%/s represents a rate of loading that is very slow in terms of physiological activities. At this rate, the interstitial fluid in the reserve zone has adequate time to cross the calcified cartilage border and the proliferative zone interface during application of the load so that the tissue permeability differences provide little overall fluid resistance to tissue compression. It is also a slow enough rate of loading for intracellular fluid to be squeezed out of the cell during the application of the load. Changes in CC permeability in our simulations had almost no influence on the cellular strains at this slow loading rate. The slight decrease in strains with depth within the reserve zone was due to the higher permeability of the PZ/HZ tissue allowing interstitial fluid to more easily flow toward the metaphyseal end. Fluid flowed out of the cell at the highest velocities for the cell closest to the CC at the 5%/s strain rate (Fig. 8), corresponding to when the greatest cell deformation and maximum principal strains within the cell occurred. At this strain rate, all the cell strain measures decreased through the depth of the RZ, as the transmembrane fluid velocity decreased with depth in the RZ and reached minimum values for the cell nearest the PZ. As stated in the previous section, the outflow velocity of the ECM interstitial fluid across the RZ borders is much greater at 5%/s than at 0.18%/s (Fig. 7b). The fluid

pressure differential between the interior and exterior of the chondrocyte at the CC border is sufficient to cause fluid to leave the cell at a relatively high velocity after 0.9 s of ramp loading (5%/s) compared with the slowest applied loading rate of 0.18%/s after 25 s of ramp loading. As the applied loading rates increase, the fluid velocity across the RZ/CC and PZ interfaces continues to increase (Fig. 7b) maintaining approximately uniform fluid pressures in the RZ (Fig. 2), but less time is available for fluid to exit the cell and the transmembrane velocities begin to decrease. At the highest strain rate of 200%/s, for a ramp period of 0.0225 s, the transmembrane fluid velocity across the cell membrane drops to nearly zero (Fig. 8). At this loading rate, the observed pattern of cellular maximum principal strains and height and width strain increasing with depth within the RZ is similar to those obtained from a previously published single-phase elastic model of in situ chondrocytes in the RZ (Kazemi and Williams 2019).

The fluid boundary condition at the reserve zone-calcified cartilage interface has a notable effect on our results. It had the highest influence on the cell-level strains for the chondrocyte close to CC border. This implies that this reserve zone cell is the most sensitive to the permeability boundary condition and this cell strain sensitivity to CC permeability decreases with distance from that border. The assumption of a lower permeable CC may represent an extreme case of boundary permeability when the cartilage is close to fusing at the end of growth when a stiff dense subchondral bone plate has formed at the epiphyseal border. Such dense bone provides a continuous layer, acting as a barrier to fluid flow and could shut off fluid exchange (Cohen et al. 1994). The structural and mechanical properties of cartilage and its borders with the bone change during skeletal development (Mow and Guo 2002; Wosu et al. 2012). In early stages of growth, the epiphyseal border between cancellous bone and the reserve zone is open and a thin layer of bone with many perforations for blood vessels provides for a more highly permeable interface with bone marrow spaces than in the established growth plate at later stages. The compositional and structural variations influence the ability of interstitial fluid to flow through the matrix and consequent change of fluid flow pathway, which affects the permeability of cartilage chondro-osseous junctions (Berteau et al. 2016; Maroudas et al. 1968; Mow and Guo 2002). There are not enough studies on the permeability of the growth plate and chondro-osseous junctions to inform us on how they change during skeletal development, so we treated this by considering two levels of permeability.

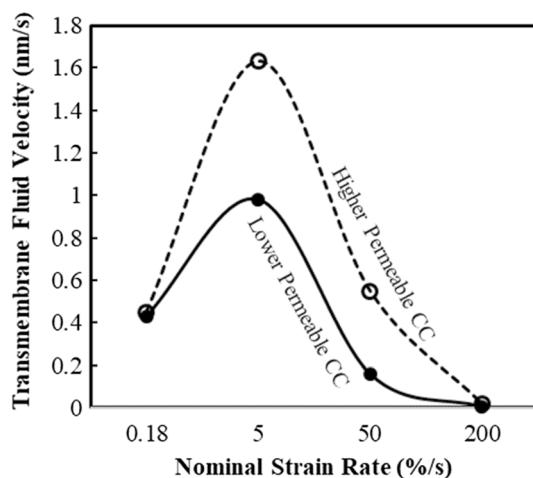


**Fig. 8** Peak transmembrane fluid outflow velocity in nanometers/s for the RZ cell closest to the calcified cartilage (CC)

#### 4.4 Depth-dependent pattern of flow-induced shear stress

The fluid flow around the cell and across the cell membrane generated shear stresses on the surface of the cell, which vary over the cell surface, with strain rates, and through the cartilage depth (RZ). The highest values of fluid-flow-induced shear stress occurred for the cell location closest to the CC, where it ranged from  $2 \times 10^{-3}$  Pa at 0.18%/s, increasing steadily to  $8 \times 10^{-3}$  Pa at 200%/s (Fig. 6). For the cell at greater distance from the CC and near the PZ, the highest fluid shear stress is less than  $10^{-3}$  Pa and occurred at the cell equator (90 degrees), for the cell at a tissue depth between the CC and PZ at lowest strain rate; and at the cell north pole (0 degrees) for the cell at the PZ border at the highest strain rate.

To our knowledge, this is the first study to calculate interstitial fluid shear stresses around chondrocytes in growth plate cartilage. It is difficult to evaluate the stimulatory effect of these shear stresses *in situ*. Interstitial fluid shear stresses through articular cartilage have been estimated from computational simulations of stress relaxation experiments to be as high as  $65 \times 10^{-3}$  Pa for 15% compression at 5%/s (Ateshian et al. 2007) using a different method for calculating fluid shear stress. The fluid shear stress reported by Ateshian et al. was calculated assuming a Brinkman transition layer by the equation  $\tau = w_{\infty} \sqrt{(\mu_f/k)}$ , where  $w_{\infty}$  represents the flux outside the transition layer tangential to the cell membrane as determined from the finite element analysis. *In vitro* studies on the effects of convective fluid flow around cells have, with a few exceptions, mostly considered relatively large fluid-induced shear stresses, of the order of  $100 \times 10^{-3}$  Pa or more. Shear stresses of  $100 \times 10^{-3}$  Pa have been shown to stimulate spatial heterogeneity in the deposition of collagen types I and II in 250-microns scaffold-free articular cartilage constructs that were produced *de novo* by bovine articular chondrocytes; and to increase the tensile strength and moduli of the extracellular matrix (Gemmiti and Guldborg 2009). Exposure to  $12 \times 10^{-3}$  Pa 1 Hz sinusoidal shear stress for 30 min/day, followed by steady flow at  $0.4 \times 10^{-3}$  Pa shear stress for the rest of the day, has been shown to stimulate aggrecan and type II collagen accumulation in 2-mm thick chondrocyte-seeded agarose hydrogels (Chen et al. 2012). Similarly, articular chondrocytes subjected to shear stresses of  $0.7 \times 10^{-3}$  to  $310 \times 10^{-3}$  Pa produced tissue with higher collagen II content than static controls (Gemmiti and Guldborg 2009). Interestingly, in the same study, the collagen I content of tissues formed under shear stresses between  $0.7 \times 10^{-3}$  and  $4.6 \times 10^{-3}$  Pa was the same as for static controls, but greater than controls for shear stresses above  $18.9 \times 10^{-3}$  Pa (Gemmiti and Guldborg 2009). These results suggest that lower levels of fluid shear stress may be beneficial for chondrocytes to maintain cartilage, but high levels

may induce a fibrocartilage phenotype. Considering these *in vitro* studies on articular chondrocytes, it seems possible that the convective fluid shear stresses around reserve zone chondrocytes calculated for 5% compression may fall in the stimulatory range for maintaining and producing cartilage tissue.

Considering only values of fluid shear stress in the possibly stimulatory range of  $0.4 \times 10^{-3}$  Pa and above, it may be noted that the fluid shear stresses reached  $2\text{--}8 \times 10^{-3}$  Pa for the cell at the RZ/CC border for all loading rates;  $0.5\text{--}0.8 \times 10^{-3}$  Pa for the cell in the middle of the RZ at 0.18%/s and 200%/s, respectively; and  $0.9 \times 10^{-3}$  Pa for the cell at the RZ/PZ border only for the fastest strain rate of 200%/s. This implies a possible stratification in stimulatory fluid shear stresses by location within the RZ, as well as loading rate. Impulsive loading rates are possibly stimulatory for cells in all locations, but much more so near the CC border. Very low strain rates may also deliver stimulatory levels of shear stress to cells at the CC border and also to those in the middle of the RZ.

The predicted shear stresses in our model fall in the range of values reported to be stimulatory for producing cartilage matrix components *in vitro*. This suggests that the fluid-flow-induced shear stresses in our study may stimulate cells in the reserve zone and contribute to cell signal transduction at the loading rates examined in our study. Fluid shear stresses acting along the surfaces of cilia may also provide stimulatory signals to the cell. The location of maximum shear stress on the cell surface and the orientation of the cell may play a role in cell reorientation and cell alignment within the reserve zone to prepare the cells and for columnar alignment in the PZ (De Andrea et al. 2010). It has been suggested that resting chondrocytes produce a growth plate-orienting morphogen that diffuses into the proliferative zone, setting up a concentration gradient that guides the orientation of proliferative columns (Abad et al. 2002). It has also been proposed that reserve zone chondrocytes produce a morphogen that inhibits terminal differentiation of nearby proliferative zone chondrocytes (Abad et al. 2002), suggesting that the reserve zone may be partially responsible for the organization of the growth plate into distinct zones. The gradient in cellular strains and the fluid shear stresses at the cell surface predicted by our model may be the source of a mechanoregulatory component of such morphogens.

Little is known about the function of chondrocytes in the reserve zone, but it has recently been shown that some of the chondrocytes are similar to stem cells. Cells termed 'neocartilage cells' surrounded by a basophilic matrix near the subchondral bone plate have been observed (Kazemi and Williams 2018, 2020) that are larger than chondrocytes found in the rest of the reserve zone. These cells are found close to areas where the subchondral bone plate is perforated by marrow on one side and reserve zone

cartilage on the other and they eventually become embedded in the calcified cartilage which likely contributes to subchondral bone plate formation. The greater sensitivity of cells in this location to the CC permeability and strain rate found in the present study may have relevance to understanding the role of these cells. Reserve zone chondrocytes close to the proliferative zone contribute to cell line by either joining the cell column or by dividing and producing a daughter cell to join the cell column of the proliferative zone. It is not known which of these occur. Shear stresses of  $10^{-3}$  Pa on the surface of these cells under impact loading may be at a stimulatory level and play a role in this regard.

There are a number of limitations in this study. Our computational results were compared with stress relaxation data obtained from previous experiments on bone/growth-plate/bone plugs in terms of the time history. In these experiments, samples were compressed with a ramp function displacement at 0.18%/s nominal strain rate and held at constant displacement until the measured load equilibrated (Tutorino et al. 2001). Comparisons of our model to these data demonstrated comparable stress relaxation versus time plots and comparable tangent modulus values during ramp loading, giving us confidence that the macroscale model reproduced the overall transient response of bone/growth-plate-cartilage/bone. However, the models did not include the complex undulations of the mammillary process of cartilage-bone interfaces which are represented as idealized flat and level interfaces. Such undulations and a nonlevel interface can cause a complex state of stress within the cartilage rather than pure compression and prevent a more precise quantitative comparison between the finite element model and the experimental data. The dimensions of the model in this computational study approximate those experimental samples and may represent an idealized version of the entire growth plate in a small animal. Limitations of this study include the assumption of a homogenous solid phase for cartilage structure and absence of the collagen fiber network. The collagen network would affect the fluid flow and cell tensile strain, but we have been unable to find any definitive studies on the alignment of collagen in the growth plate reserve zone. It has been reported that collagen fibers are arranged longitudinally and transversely in the reserve zone. However, the published evidence for this is limited to photomicrographs of the region in close proximity to the perimeter of the growth plate near the perichondrium (Speer 1982), whereas our model represents a section within the interior of the growth plate away from the perichondrial boundary. We have also not taken into account the role of ions and proteoglycan fixed charge density. By assuming homogeneous isotropic properties for the PZ and HZ zone, the chondron tubular structure was ignored. Perfect bonding was assumed at all interfaces when it is likely that the cell boundaries are

not perfectly bonded to the pericellular matrix but may be attached at focal points. The surface of the cell was assumed to be smooth when it is likely to have a ruffled shape (Moo et al. 2013; Moo and Herzog 2017). The assumption of a free boundary at the radial edge of the sample may not account for the perichondrial soft tissue found in vivo which may serve as a barrier to fluid exudation and restrain the radial expansion of the growth plate cartilage, especially in the proliferative and hypertrophic zones.

## 5 Conclusions

The findings of this study are potentially important for understanding the role of the reserve zone cartilage and of the mechanical environment of reserve zone chondrocytes in the growth plate when subjected to dynamic loading conditions. The cellular strains within the reserve zone are depth-dependent and highly sensitive to the loading rate and to the permeability of the subchondral bone plate, which likely changes during development and maturation. This sensitivity to permeability decreases through reserve zone depth with distance from the epiphyseal junction. The values predicted by our model for fluid-flow-induced shear stress exceed values reported to be stimulatory to cells during in vitro experiments. The gradient observed through the depth of the reserve zone in potential mechanoregulatory signals, such as cell strain, membrane strain, intracellular fluid pressure, and fluid shear stress varies with the rate of loading. The depth-dependent patterns at very slow quasi-static loading rates and at high impact loading rates differ from those observed during intermediate loading rates. This is explained by the biphasic nature of the tissue in which the fluid component plays a more dominant role in supporting loads at higher loading rates. These strain rate-dependent gradients in the microenvironment of the cells may provide necessary signals for the hypothesized regulatory role of the reserve zone cartilage.

**Acknowledgements** We thank Dr. Eng Kuan Moo at the University of Calgary for his help with computational implementation.

## Declarations

**Conflict of interest** The authors have no conflicts of interest to declare that are relevant to the content of this article.

## References

- Abad V, Meyers JL, Weise M, Gafni RI, Barnes KM, Nilsson O, Baron J (2002) The role of the resting zone in growth plate

- chondrogenesis. *Endocrinology* 143(5):1851–1857. <https://doi.org/10.1210/endo.143.5.8776>
- Accadbled F, Laffosse JM, Ambard D, Gomez-Brouchet A, De Gauzy JS, Swider P (2008) Influence of location, fluid flow direction, and tissue maturity on the macroscopic permeability of vertebral end plates. *Spine* 33(6):612–619. <https://doi.org/10.1097/BRS.0b013e318166e0d7>
- Alexopoulos LG, Setton LA, Guilak F (2005) The biomechanical role of the chondrocyte pericellular matrix in articular cartilage. *Acta Biomater* 1(3):317–325. <https://doi.org/10.1016/j.actbio.2005.02.001>
- Argote PF, Kaplan JT, Poon A, Xu X, Cai L, Emery NC, Neu CP (2019) Chondrocyte viability is lost during high-rate impact loading by transfer of amplified strain, but not stress, to pericellular and cellular regions. *Osteoarthritis Cartilage* 27(12):1822–1830. <https://doi.org/10.1016/j.joca.2019.07.018>
- Ateshian GA, Costa KD, Hung CT (2007) A theoretical analysis of water transport through chondrocytes. *Biomech Model Mechanobiol* 6:91–10
- Berteau JP, Oyen M, Shefelbine SJ (2016) Permeability and shear modulus of articular cartilage in growing mice. *Biomech Model Mechanobiol* 15(1):205–212. <https://doi.org/10.1007/s10237-015-0671-3>
- Bries AD, Weiner DS, Jacquet R, Adamczyk MJ, Morscher MA, Lowder E, Askew MJ, Steiner RP, Horne WI, Landis WJ (2012) A study in vivo of the effects of a static compressive load on the proximal tibial physis in rabbits. *J Bone Joint Surg* 94(15):e111. <https://doi.org/10.2106/JBJS.K.00340>
- Cancel M, Grimard G, Thuillard-Crisinel D, Moldovan F, Villemure I (2009) Effects of in vivo static compressive loading on aggrecan and type II and X collagens in the rat growth plate extracellular matrix. *Bone* 44(2):306–315. <https://doi.org/10.1016/j.bone.2008.09.005>
- Carter DR, Wong M (1988) Mechanical stresses and endochondral ossification in the chondroepiphysis. *J Orthop Res* 6(1):148–154. <https://doi.org/10.1002/jor.1100060120>
- Carter DR, Mikić B, Padian K (1998) Epigenetic mechanical factors in the evolution of long bone epiphyses. *Zool J Linn Soc* 123(2):163–178. <https://doi.org/10.1111/j.1096-3642.1998.tb01298.x>
- Chen T, Buckley M, Cohen I, Bonassar L, Awad HA (2012) Insights into interstitial flow, shear stress, and mass transport effects on ECM heterogeneity in bioreactor-cultivated engineered cartilage hydrogels. *Biomech Model Mechanobiol* 11(5):689–702. <https://doi.org/10.1007/s10237-011-0343-x>
- Cohen B, Chorney GS, Phillips DP, Dick HM, Mow VC (1994) Compressive stress-relaxation behavior of bovine growth plate may be described by the nonlinear biphasic theory. *J Orthop Res* 12(6):804–813. <https://doi.org/10.1002/jor.1100120608>
- Cohen B, Lai WM, Mow VC (1998) A transversely isotropic biphasic model for unconfined compression of growth plate and chondroepiphysis. *ASME J Biomech Eng* 120(4):491–496. <https://doi.org/10.1115/1.2798019>
- De Andrea CE, Wiweger M, Prins F, Bovée JV, Romeo S, Hogenboom PC (2010) Primary cilia organization reflects polarity in the growth plate and implies loss of polarity and mosaicism in osteochondroma. *Lab Invest* 90(7):1091–1101. <https://doi.org/10.1038/labinvest.2010.81>
- Eberhardt AW, Keer LM, Lewis JL, Vithoontien V (1990) An analytical model of joint contact. *ASME J Biomech Eng* 112(4):407–413. <https://doi.org/10.1115/1.2891204>
- Fan C, Cool JC, Scherer MA, Foster BK, Shandala T, Tapp H, Xian CJ (2009) Damaging effects of chronic low-dose methotrexate usage on primary bone formation in young rats and potential protective effects of folic acid supplementary treatment. *Bone* 44(1):61–70. <https://doi.org/10.1016/j.bone.2008.09.014>
- Farzaneh S, Paseta O, Gómez-Benito MJ (2015) Multi-scale finite element model of growth plate damage during the development of slipped capital femoral epiphysis. *Biomech Model Mechanobiol* 14(2):371–385. <https://doi.org/10.1007/s10237-014-0610-8>
- Ficklin TP, Davol A, Klisch SM (2009) Simulating the growth of articular cartilage explants in a permeation bioreactor to aid in experimental protocol design. *ASME J Biomech Eng* 131(4):041008. <https://doi.org/10.1115/1.3049856>
- Frost HM (1990) Skeletal structural adaptations to mechanical usage (SATMU): 3. The hyaline cartilage modeling problem. *Anatom Rec* 226(4):423–432. <https://doi.org/10.1002/ar.1092260404>
- Gao J, Williams JL, Roan E (2014) On the state of stress in the growth plate under physiologic compressive loading. *Open Journal of Biophysics* 4(1):13–21. <https://doi.org/10.4236/ojbiphys.2014.41003>
- Gao J, Roan E, Williams JL (2015) Regional variations in growth plate chondrocyte deformation as predicted by three-dimensional multiscale simulations. *PLoS ONE* 10(4):e0124862. <https://doi.org/10.1371/journal.pone.0124862>
- Gao J, Williams JL, Roan E (2017) Multiscale modeling of growth plate cartilage mechanobiology. *Biomech Model Mechanobiol* 16(2):667–679. <https://doi.org/10.1007/s10237-016-0844-8>
- Gemmiti CV, Gulberg RE (2009) Shear stress magnitude and duration modulates matrix composition and tensile mechanical properties in engineered cartilaginous tissue. *Biotechnol Bioeng* 104(4):809–820. <https://doi.org/10.1002/bit.22440>
- Grimm MJ, Williams JL (1997) Measurements of permeability in human calcaneal trabecular bone. *J Biomech* 30(7):743–745. [https://doi.org/10.1016/S0021-9290\(97\)00016-X](https://doi.org/10.1016/S0021-9290(97)00016-X)
- Guharay F, Sachs F (1984) Stretch-activated single ion channel currents in tissue-cultured embryonic chick skeletal muscle. *J Physiol* 352(1):685–701. <https://doi.org/10.1113/jphysiol.1984.sp015317>
- Guilak F, Mow VC (2000) The mechanical environment of the chondrocyte: a biphasic finite element model of cell–matrix interactions in articular cartilage. *J Biomech* 33(12):1663–1673. [https://doi.org/10.1016/S0021-9290\(00\)00105-6](https://doi.org/10.1016/S0021-9290(00)00105-6)
- Gupta T, Donahue TLH (2006) Role of cell location and morphology in the mechanical environment around meniscal cells. *Acta Biomater* 2(5):483–492. <https://doi.org/10.1016/j.actbio.2006.05.009>
- Hallett SA, Ono W, Ono N (2019) Growth plate chondrocytes: skeletal development, growth and beyond. *Int J Mol Sci* 20(23):6009. <https://doi.org/10.3390/ijms20236009>
- Hwang J, Bae WC, Shieu W, Lewis CW, Bugbee WD, Sah RL (2008) Increased hydraulic conductance of human articular cartilage and subchondral bone plate with progression of osteoarthritis. *Arthritis Rheumat Off J Am College Rheumatol* 58(12):3831–3842. <https://doi.org/10.1002/art.24069>
- Kazemi M, Williams JL (2018) On the role of the reserve zone and mechano-regulatory stimuli in the development and maturation of the growth plate: Observations and models. Manuscript submitted for publication.
- Kazemi M, Williams JL (2018) Elemental and histological study of the growth plate reserve zone–subchondral bone interface. Paper presented at: Orthopaedic Research Society Annual Meeting (ORS), 2018; New Orleans, LA.
- Kazemi M, Williams JL (2019) Chondrocyte and pericellular matrix deformation and strain in the growth plate cartilage reserve zone under compressive loading. In: *International Symposium on Computer Methods in Biomechanics and Biomedical Engineering* (pp. 526–538). Springer, Cham. [https://doi.org/10.1007/978-3-030-43195-2\\_43](https://doi.org/10.1007/978-3-030-43195-2_43)
- Kazemi M, Williams JL (2020) Properties of cartilage-subchondral bone junctions: a narrative review with specific focus on the

- growth plate. Cartilage. <https://doi.org/10.1177/1947603520924776>
- Komeili A, Otoo BS, Abusara Z, Sibole S, Federico S, Herzog W (2020) Chondrocyte deformations under mild dynamic loading conditions. *Ann Biomed Eng.* <https://doi.org/10.1007/s10439-020-02615-9>
- Lacroix D, Prendergast PJ, Li G, Marsh D (2002) Biomechanical model to simulate tissue differentiation and bone regeneration: application to fracture healing. *Med Biol Eng Compu* 40(1):14–21. <https://doi.org/10.1007/BF02347690>
- Lai WM, Mow VC (1980) Drag-induced compression of articular cartilage during a permeation experiment. *Biorheology* 17(1–2):111–123. <https://doi.org/10.3233/BIR-1980-171-213>
- Lai WM, Mow VC, Roth V (1981) Effects of nonlinear strain-dependent permeability and rate of compression on the stress behavior of articular cartilage. *ASME J Biomech Eng* 103(2):61–66. <https://doi.org/10.1115/1.3138261>
- Lavagnino M, Arnoczky SP, Kepich E, Caballero O, Haut RC (2008) A finite element model predicts the mechanotransduction response of tendon cells to cyclic tensile loading. *Biomech Model Mechanobiol* 7(5):405–416. <https://doi.org/10.1007/s10237-007-0104-z>
- Leipzig ND, Athanasiou KA (2008) Static compression of single chondrocytes catabolically modifies single-cell gene expression. *Biophys J* 94(6):2412–2422. <https://doi.org/10.1529/biophysj.107.114207>
- Lui JC (2020) Home for a rest: stem cell niche of the postnatal growth plate. *J Endocrinol* 246(1):R1–R11. <https://doi.org/10.1530/JOE-20-0045>
- Maroudas A, Bullough P, Swanson SAV, Freeman MAR (1968) The permeability of articular cartilage. *The Journal of bone and joint surgery.* 50(1):166–177. <https://doi.org/10.1302/0301-620X.50B1.166> (**British volume**)
- Matsushita Y, Ono W, Ono. (2020) Growth plate skeletal stem cells and their transition from cartilage to bone. *Bone* 136:115359. <https://doi.org/10.1016/j.bone.2020.115359>
- Moo EK, Herzog W (2017) Unfolding of membrane ruffles of in situ chondrocytes under compressive loads. *J Orthop Res* 35(2):304–310
- Moo EK, Herzog W, Han SK, Osman N, Pingguan-Murphy B, Federico S (2012) Mechanical behavior of in-situ chondrocytes subjected to different loading rates: a finite element study. *Biomech Model Mechanobiol* 11(7):983–993. <https://doi.org/10.1007/s10237-011-0367-2>
- Moo EK, Amrein M, Epstein M, Duvall M, Osman NAA, Pingguan-Murphy B, Herzog W (2013) The properties of chondrocyte membrane reservoirs and their role in impact-induced cell death. *Biophys J* 105(7):1590–1600. <https://doi.org/10.1016/j.bpj.2013.08.035>
- Moo EK, Han SK, Federico S, Sibole SC, Jinha A, Osman NAA, Herzog W (2014) Extracellular matrix integrity affects the mechanical behavior of in-situ chondrocytes under compression. *J Biomech* 47(5):1004–1013. <https://doi.org/10.1016/j.jbiomech.2014.01.003>
- Morris CE, Sigurdson W (1989) Stretch-inactivated ion channels coexist with stretch-activated ion channels. *Science* 243(4892):807–809. <https://doi.org/10.1126/science.2536958>
- Mow VC, Guo XE (2002) Mechano-electrochemical properties of articular cartilage: their inhomogeneities and anisotropies. *Annu Rev Biomed Eng* 4(1):175–209. <https://doi.org/10.1146/annurev.bioeng.4.110701.120309>
- Mow VC, Kuei SC, Lai WM, Armstrong CG (1980) Biphasic creep and stress relaxation of articular cartilage in compression: theory and experiments. *ASME J Biomech Eng* 102(1):73–84. <https://doi.org/10.1115/1.3138202>
- Mow VC, Hou JS, Owens JM, Ratcliffe A (1990) Biphasic and quasi-linear viscoelastic theories for hydrated soft tissues. In: *Biomechanics of diarthrodial joints* (pp. 215–260). Springer, New York, NY. [https://doi.org/10.1007/978-1-4612-3448-7\\_8](https://doi.org/10.1007/978-1-4612-3448-7_8).
- Nauman EA, Fong KE, Keaveny TM (1999) Dependence of intertrabecular permeability on flow direction and anatomic site. *Ann Biomed Eng* 27(4):517–524. <https://doi.org/10.1114/1.195>
- Nguyen BV, Wang QG, Kuiper NJ, El Haj AJ, Thomas CR, Zhang Z (2010) Biomechanical properties of single chondrocytes and chondrons determined by micromanipulation and finite-element modelling. *J R Soc Interface* 7(53):1723–1733. <https://doi.org/10.1098/rsif.2010.0207>
- Pauwels F (1960) Eine neue Theorie über den Einfluß mechanischer Reize auf die Differenzierung der Stützgewebe. *Z Anat Entwickl* 121(6):478–515. <https://doi.org/10.1007/BF00523401>
- Pérez del Palomar A, Doblaré M (2006) On the numerical simulation of the mechanical behavior of articular cartilage. *Int J Numer Meth Eng* 67(9):1244–1271. <https://doi.org/10.1002/nme.1638>
- Poole CA, Flint MH, Beaumont BW (1987) Chondrons in cartilage: ultrastructural analysis of the pericellular microenvironment in adult human articular cartilages. *J Orthop Res* 5(4):509–522. <https://doi.org/10.1002/jor.1100050406>
- Radhakrishnan P, Lewis NT, Mao JJ (2004) Zone-specific micromechanical properties of the extracellular matrices of growth plate cartilage. *Ann Biomed Eng* 32(2):284–291. <https://doi.org/10.1023/B:ABME.0000012748.41851.b4>
- Sakai N, Hagihara Y, Hashimoto C, Komori M, Sawae Y, Murakami T (2015) An estimation of mechanical properties of articular cartilage for biphasic finite element analyses. *J Biomech Sci Eng* 10(4):15–00228. <https://doi.org/10.1299/jbse.15-00228>
- Seeger-Nukpezah T, Golemis EA (2012) The extracellular matrix and ciliary signaling. *Curr Opin Cell Biol* 24(5):652–661. <https://doi.org/10.1016/j.ceb.2012.06.002>
- Sergerie K, Lacoursière MO, Lévesque M, Villemure I (2009) Mechanical properties of the porcine growth plate and its three zones from unconfined compression tests. *J Biomech* 42(4):510–516. <https://doi.org/10.1016/j.jbiomech.2008.11.026>
- Shao YY, Wang L, Welter JF, Ballock RT (2012) Primary cilia modulate Ihh signal transduction in response to hydrostatic loading of growth plate chondrocytes. *Bone* 50(1):79–84. <https://doi.org/10.1016/j.bone.2011.08.033>
- Shelfelbine SJ, Carter DR (2004) Mechanobiological predictions of growth front morphology in developmental hip dysplasia. *J Orthop Res* 22(2):346–352. <https://doi.org/10.1016/j.orthres.2003.08.004>
- Soltz MA, Ateshian GA (1998) Experimental verification and theoretical prediction of cartilage interstitial fluid pressurization at an impermeable contact interface in confined compression. *J Biomech* 31(10):927–934. [https://doi.org/10.1016/S0021-9290\(98\)00105-5](https://doi.org/10.1016/S0021-9290(98)00105-5)
- Song Y, Lee D, Shin CS, Carter DR, Giori NJ (2013) Physeal cartilage exhibits rapid consolidation and recovery in intact knees that are physiologically loaded. *J Biomech* 46(9):1516–1523. <https://doi.org/10.1016/j.jbiomech.2013.03.026>
- Speer DP (1982) Collagenous architecture of the growth plate and perichondrial ossification groove. *J Bone Joint Surg* 64(3):399–407. <https://doi.org/10.2106/00004623-198264030-00010> (**American volume**)
- Stender ME, Regueiro RA, Ferguson VL (2017) A poroelastic finite element model of the bone–cartilage unit to determine the effects of changes in permeability with osteoarthritis. *Comput Methods Biomech Biomed Engin* 20(3):319–331. <https://doi.org/10.1080/10255842.2016.1233326>
- Sylvestre PL, Villemure I, Aubin CE (2007) Finite element modeling of the growth plate in a detailed spine model. *Med*



- Biol Eng Compu 45(10):977–988. <https://doi.org/10.1007/s11517-007-0220-z>
- Tutorino, JC, Khubchandani, ZG, Williams, JL, Cobb, CM and Schmidt, TL (2001). Can the epiphyseal growth plate be injured in compression? In 47th Annual Meeting of Orthopaedic Research Society (p. 353).
- Williams JL, Do PD, Eick JD, Schmidt TL (2001) Tensile properties of the physis vary with anatomic location, thickness, strain rate and age. *J Orthop Res* 19(6):1043–1048. [https://doi.org/10.1016/S0736-0266\(01\)00040-7](https://doi.org/10.1016/S0736-0266(01)00040-7)
- Wosu R, Sergerie K, Lévesque M, Villemure I (2012) Mechanical properties of the porcine growth plate vary with developmental stage. *Biomech Model Mechanobiol* 11(3–4):303–312. <https://doi.org/10.1007/s10237-011-0310-6>
- Wu JZ, Herzog W (2000) Finite element simulation of location- and time-dependent mechanical behavior of chondrocytes in unconfined compression tests. *Ann Biomed Eng* 28(3):318–330. <https://doi.org/10.1114/1.271>
- Wu JZ, Herzog W, Epstein M (1997) Evaluation of the finite element software ABAQUS for biomechanical modelling of biphasic tissues. *J Biomech* 31(2):165–169. [https://doi.org/10.1016/S0021-9290\(97\)00117-6](https://doi.org/10.1016/S0021-9290(97)00117-6)
- Yellowley CE, Jacobs CR, Li Z, Zhou Z, Donahue HJ (1997) Effects of fluid flow on intracellular calcium in bovine articular chondrocytes. *Am J Physiol Cell Physiol* 273(1):C30–C36. <https://doi.org/10.1152/ajpcell.1997.273.1.C30>

**Publisher's Note** Springer Nature remains neutral with regard to jurisdictional claims in published maps and institutional affiliations.